Effect of water treatment on microstructure and magnon thermal transport in spin ladder compound $Sr_{12}Y_2Cu_{24}O_{41}$

Shuchen Li [a], Xi Chen [a*]

[a] *Department of Electrical and Computer Engineering, University of California, Riverside, California, 92521, United States*

[*]Corresponding author: xichen@ucr.edu

Abstract

The spin ladder compounds $(Sr,Ca,La,Y)_{14}Cu_{24}O_{41}$, known for their large magnon thermal conductivity, show great promise for thermal management and spin caloritronic applications. However, these materials are unstable in humid air and can decompose when exposed to moisture. The effect of decomposition on magnon thermal transport in these materials remains unreported. Understanding this effect is crucial for developing spin ladder compounds for practical applications. This study highlights the distinct impact of water treatment on the microstructure and thermal transport properties in single crystals and polycrystals of the spin ladder compound $Sr_{12}Y_2Cu_{24}O_{41}$. Our findings indicate that water treatment substantially decreases the magnon thermal conductivity of polycrystals, while the magnon thermal conductivity of single crystals remains largely unaffected. This significant difference can be attributed to the presence of grain boundaries in polycrystals, which allow water to penetrate the bulk of the polycrystalline samples. The reaction with water results in the formation of CuO and $SrCO_3$ nanostructures, which scatter both phonons and magnons, thereby reducing both lattice and magnon thermal conductivity. To mitigate the adverse effects of water interaction, we developed a simple sputter coating method for spin ladder samples. Notably, the metal-coated samples demonstrated sustained high thermal conductivity, even after extended exposure to water treatment. Our study provides useful insights into the practical applications of the cuprate-based quantum magnets in thermal management and energy conversion.

Introduction

The search for thermally conductive materials is a critical area of research in thermal management of microelectronic devices.[1–5] As electronic components become smaller and more powerful, managing heat dissipation is essential to maintain performance and prevent overheating, which can lead to device failure. Numerous materials have been identified as promising candidates for thermal management, primarily utilizing conventional mechanisms of thermal transport mediated by phonons (lattice vibrations) or electrons.[6–10] These materials rely on the established understanding that phonons and electrons are the primary heat carriers in most solids, contributing significantly to their thermal properties. Besides these conventional heat carriers, magnons, as the quasiparticles of spin waves, can carry a large amount of heat due to their substantial group velocity.[11,12] Significant magnetic thermal transport has been discovered in various quantum magnets with strong magnetic couplings.[13–17] Furthermore, as magnons can be manipulated by external magnetic or electric field, the magnon thermal transport is more sensitive to the external fields, compared to the phonon-mediated thermal transport.[18–20] This behavior enables an active control on the thermal conductivity (κ) in magnetic materials, functioning as a thermal switch.[21,22] Furthermore, magnons have been extensively studied in relation to the spin Seebeck effect[23–25] and magnon-

drag-enhanced Seebeck effect,[26–28] showing promising potential for thermoelectric energy conversion applications. However, the study of magnon thermal transport remains relatively unexplored compared to the conventional heat carriers such as phonons and electrons, making it an important avenue for further research. Among the current studies on quantum magnets, the spin ladder compounds $(Sr,Ca,La,Y)_{14}Cu_{24}O_{41}$ have demonstrated the largest magnon thermal conductivity (κ_M) around room temperature.[13,29–31] This finding makes them an excellent platform for exploring practical thermal management applications in microelectronic devices. Furthermore, the manipulation of magnon thermal transport in spin ladder compounds has already been demonstrated for developing thermal switches,[22] which are highly relevant for advanced thermal management technologies.

The large magnon thermal conductivity in the spin ladder compounds can be attributed to their strong antiferromagnetic couplings of around 170 meV.[11] A peak magnon thermal conductivity of around 70 W m^{-1} K^{-1} at 150 K has been observed in the undoped spin ladder $Sr_{14}Cu_{24}O_{41}$.[29,31] Compared with the gapless magnon dispersion in the ferromagnetic crystal,[32] previous neutron scattering studies on spin ladder compounds have revealed a large energy gap of around 32.5 meV in the magnon dispersion.[11,33] This large energy gap thermally freezes magnons at low temperatures, leading to negligible magnon contributions to thermal transport below 50 K. This behavior is also observed in other cuprate compounds,[34–36] making them ideal platforms for studying magnon thermal transport as magnon and phonon contributions can be easily distinguished. It has been reported that chemical doping can modify the magnon thermal transport in spin ladder compounds.[13,37,38] As an intrinsically hole-doped compound, the magnon thermal transport in $Sr_{14}Cu_{24}O_{41}$ is affected by magnon-hole scattering. Substituting Sr ions with La or Y ions, which have a higher valence state than Sr ions, can effectively reduce hole concentration, suppress magnon-hole scattering, and enhance magnon thermal conductivity.[13,31,38] For example, the room-temperature magnon thermal conductivity of single crystals increases from 7 W m^{-1} K^{-1} for $Sr_{14}Cu_{24}O_{41}$ to 19 W m^{-1} K^{-1} for $Sr_{12}Y_2Cu_{24}O_{41}$.[38] On the other hand, Ca doping can increase the hole concentration in the ladder layers by transferring holes from the chain layers.[13,31] Thereby, it enhances magnon-hole scattering and suppresses magnon thermal transport.[39] Furthermore, the effect of nanostructuring on magnon thermal transport has been studied on spin ladder polycrystals and microrods.[40–43] The increased grain boundaries and defects cause a strong scattering on transport of magnons and other particles (or quasiparticles),[44] leading to a suppression of magnon thermal conductivity.

While magnon thermal transport has been reported for about two decades in the cuprate-based spin ladder compounds,[15,16,29,34,39,45] the real-world application of these magnetic insulators still faces a challenge. The spin ladder compounds decompose under a humid environment,[46] which may increase magnon scattering and potentially reduce magnon thermal conductivity.[33] However, the actual effects of the decomposition on the magnon thermal transport in the spin ladder compounds have not yet been thoroughly investigated. Therefore, understanding the environmental stability of these materials is crucial for their practical application. Humidity and exposure to water are often unavoidable in real-world conditions, making it crucial to investigate the effects of water treatment on magnon thermal transport. Additionally, there is a pressing need to develop effective strategies to prevent water-induced degradation, thereby enabling broader applications of spin ladder compounds.

In this work, we investigate the detrimental effects of water exposure on the microstructure and thermal conductivity of both polycrystalline and single crystal spin ladder compound $Sr_{12}Y_2Cu_{24}O_{41}$. The reaction of spin ladder compound with water causes two different particle morphologies in the polycrystal. Near the

surface, the decomposition process induces the formation of $SrCO_3$ nanorods, while the nanoparticles of CuO and $SrCO_3$ are generated in the center of the sample. As the water treatment duration increases, the increased concentration of nanostructures causes a stronger scattering on magnons and suppresses the magnon thermal conductivity by approximately 50% at 300 K in the sample with 4 h of water treatment. On the other hand, the single crystal $Sr_{12}Y_2Cu_{24}O_{41}$ exhibits minimal changes in thermal conductivity after water treatment, due to its limited reaction with water at the sample's core. This behavior can be attributed to the absence of grain boundaries in the single crystal. Furthermore, we developed a simple and effective metal-coating method using elemental gold to prevent water-induced degradation of polycrystalline samples. With the protection of sputtered gold layer, negligible changes in thermal conductivity can be observed with water treatment up to 50 h. This method not only ensures the stability of the material but also addresses a critical barrier to the practical implementation of spin-ladder compounds in thermal management systems. Our study provides useful insights into both the fundamental understanding of magnon thermal transport and the practical considerations necessary for deploying these materials in thermal management and energy conversion applications.

Experimental Methods

Synthesis of Materials

The powders of the spin ladder compound $Sr_{12}Y_2Cu_{24}O_{41}$ were synthesized by the solid-state reaction (SSR) with the starting materials of $SrCO_3$ (purity: 99.9%, Sigma-Aldrich), Y_2O_3 (purity: 99.99%, Thermo Scientific), and CuO (purity: 99.7%, Thermo Scientific). These starting materials were mixed with the atomic ratio as Sr: Y: Cu = 12:2:24 and sintered at 940 °C for 24 h. The pellets of polycrystalline samples were prepared by consolidating the powders with cold pressing under a pressure of 330 MPa and followed by annealing at 940 °C for 12 h. The pellets were cut into bar-shaped samples of approximately $1\times1\times6$ mm^3 in size, oriented perpendicular to the pressing direction, for the thermal measurements. To prevent the reaction of water, a gold coating was applied on one polycrystalline sample with a Cressington 108 manual sputter coater.

The single crystalline sample was grown by the traveling solvent floating zone (TSFZ) method using a Quantum Design's 2-mirror IR image furnace (model: IRF01-001-05), as described in a previous report.[47] The feed and seed rods were made with the same powders as the polycrystalline samples. The solvent pellets were made with the same starting materials as polycrystalline samples with the atomic ratio of Cu: (Sr,Y) = 85: 15, where Sr: Y matched that of the feed rod. The TSFZ growth was carried out under an oxygen pressure of 1 bar, with a growth rate of 0.8 mm per hour, and a rotation speed of 30 rpm for feed and seed rods in opposite directions.

The water treatment was applied on the samples by submerging the samples in deionized water. After the treatment, the samples were dried at 100 °C for 4 h in air. The density of samples was measured by the Archimedes method.[41] The untreated polycrystalline sample shows a density of 4.7 g cm^{-3}. The density increases to 5.2 and 5.3 g cm^{-3} after 4 and 10 h of water treatment. This increase in density can be attributed to the formation of CuO, which has a larger density of 6.3 g cm^{-3}.

Characterization of Phase and Microstructure

The phase purity and crystal structure of the samples were characterized using a PANalytical Empyrean Series 2 X-ray diffraction (XRD) machine with Cu Kα (λ = 1.54 Å) radiation. The microstructure and

composition of polycrystalline samples were studied by a TESCAN Vega3 SBH scanning electron microscopy (SEM) with energy dispersive X-ray spectrometry (EDS). The orientation of the single crystal sample was characterized by single-crystal XRD with a Bruker D8 Venture equipped with a PhotonIII detector using Mo Kα (λ = 0.71073 Å) IμS micro-source for face indexing, as reported in a previous study.[38]

Thermal and Electrical Property Measurements

The thermal conductivity and Seebeck coefficient (*S*) of the spin ladder samples were measured by Quantum Design's physical property measurement system (PPMS) with the continuous mode under a continuous heating rate of 0.3 K min^{-1} in the temperature range of 5-300 K. The measurements were performed on the bar-shaped samples for both polycrystals and single crystals. The thermal conductivity of single crystals was measured along the spin ladder direction.[48] The details for the uncertainty analysis of thermal conductivity can be found in a previous study.[48]

Results and discussion

Effect of water treatment on phase and microstructure of uncoated $Sr_{12}Y_2Cu_{24}O_{41}$

The spin ladder compound $Sr_{12}Y_2Cu_{24}O_{41}$ has a layered structure within an orthorhombic unit cell and belongs to the space group *Fmmm*,[49] as shown in Fig. 1a. It is composed of CuO_2 spin chain and Cu_2O_3 spin ladder layers, with the chains of Sr and Y ions inserted between these layers. While the spin chain and spin ladder layers are stacked alternatively along *b*-axis, within the Cu_2O_3 spin ladder layer, the 180° Cu-O-Cu couplings lead to strong antiferromagnetic interactions along *a*- and *c*-axis. As a quasi-one-dimensional structure, magnon transport appears only along *c*-axis. The composition of $Sr_{12}Y_2Cu_{24}O_{41}$ was chosen because Y doping can lead to an enhanced magnon thermal conductivity due to reduced magnon-hole scattering as reported in our previous study.[38]

The powder XRD patterns of the spin ladder compound before and after 1, 4, and 10 h of water treatment are illustrated in Fig. 1b. In the pristine sample, the major peaks are consistent with calculated peaks for $Sr_{14}Cu_{24}O_{41}$ (PDF#48-1496). Compared with the pristine sample, several additional peaks can be observed in the water-treated samples, which can be identified as $SrCO_3$ and CuO. In the 1 h sample, CuO is observed as the major impurity. With the increase of treating time, the intensity of CuO peaks gradually increases. Furthermore, the peaks of $SrCO_3$ can be observed in both 4 and 10 h samples. It is noted that the peak intensity of $SrCO_3$ is much stronger in the 10 h sample. The formation of these impurities, CuO and $SrCO_3$, are due to the decomposition of the spin ladder compound in water. While the direct products of the decomposition are $Sr(OH)_2$, $Cu(OH)_2$, and $Y(OH)_3$,[46] these compounds continue to react with CO_2 during the drying process, forming $SrCO_3$, CuO, and $Y_2(CO_3)_3 \cdot 3\ H_2O$, respectively. The chemical equations of these reactions can be written as:[46]

$$Sr_{12}\ Y_2Cu_{24}O_{41} + 39\ H_2O = 12\ Sr(OH)_2 + 2\ Y(OH)_3 + 24\ Cu(OH)_2 + \ O_2 \quad (1)$$

$$Sr(OH)_2 + CO_2 = SrCO_3 + H_2O \quad (2)$$

$$Cu(OH)_2 = CuO + H_2O \quad (3)$$

$$2\ Y(OH)_3 + 3\ CO_2 = Y_2(CO_3)_3 \cdot 3\ H_2O \quad (4)$$

The XRD signals of Y-related compounds are lacking in the XRD pattern, probably due to the low Y doping level in our spin ladder compound. Additionally, the observed impurities show broad XRD peaks, indicating their small grain sizes according to the Scherrer equation.[50,51]

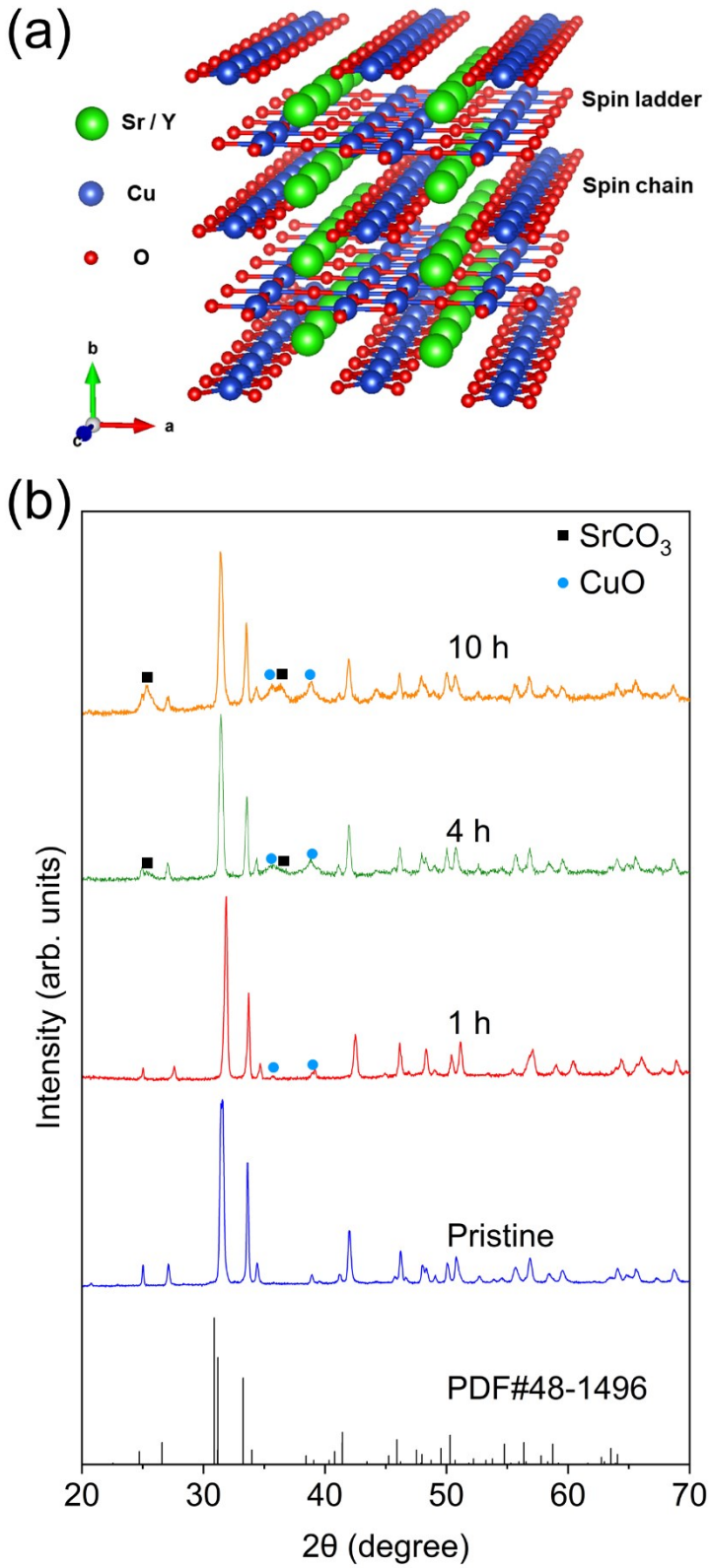

Fig. 1 (a) Crystal structure of $Sr_{12}Y_2Cu_{24}O_{41}$. (b) Powder XRD patterns of $Sr_{12}Y_2Cu_{24}O_{41}$ polycrystal samples before and after water treatment.

To investigate the impact of water treatment on the microstructures of the spin ladder compound, SEM images were taken at the center of the sample's cross section before and after treatment, as shown in Fig. 2. A notable transformation in particle morphology is observed after the treatment. Before the water treatment, most grains exhibit smooth surfaces with an average grain size of about 3 μm (Fig. 2a), which is consistent with a previous study of spin ladder compounds prepared with SSR process.[38] The well-defined grain boundaries are distinctly visible between individual grains. In contrast, after water treatment, the grain surfaces become significantly rougher, rendering the grain boundaries indistinct (Fig. 2b). Additionally, a substantial number of tiny particles, approximately 200 nm in size, are observed on the surface of grains. These small particles can be attributed to impurities such as $SrCO_3$ and CuO, which are identified in the XRD pattern.

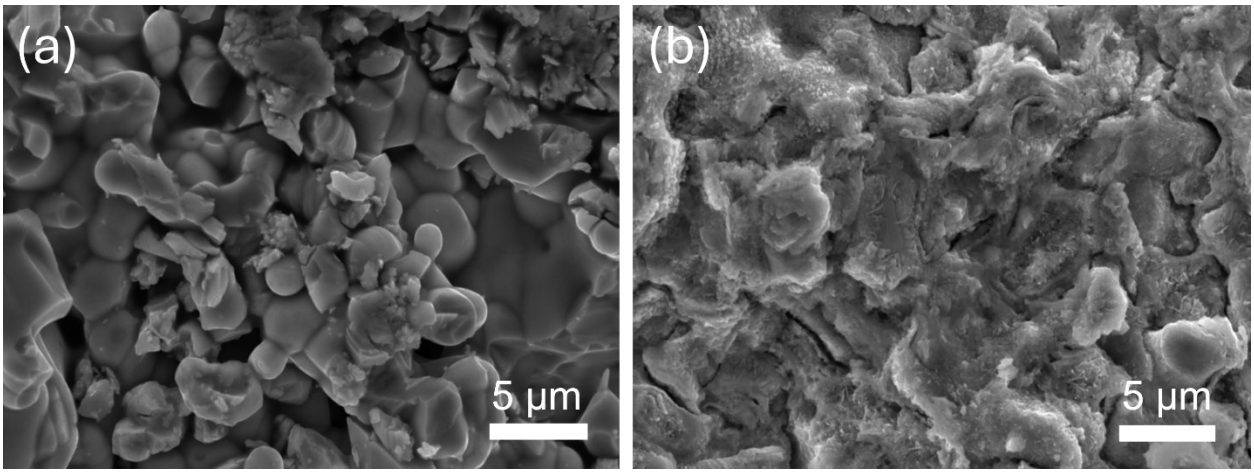

Fig. 2 SEM images at the center of cross section of the polycrystal $Sr_{12}Y_2Cu_{24}O_{41}$ (a) before and (b) after 10 h water treatment.

To further explore the mechanism of water treatment in the polycrystalline $Sr_{12}Y_2Cu_{24}O_{41}$, additional SEM images were obtained from the surface and the edge of the sample after 10 h water treatment (Fig. 3a). As displayed in Fig. 3b, the surface of the sample exhibits a severe reaction with water, as evidenced by the complete coverage of tiny particles, in contrast to the less affected central region. Fig. 3c highlights the presence of two distinct regions, each exhibiting different degrees of reaction with water. Within approximately 20 μm from the surface, numerous rod-like grains are observed. In contrast, the inner region resembles a rough grain morphology, similar to that observed in the central part of the sample. This observation of different particle morphographies suggests that water predominantly reacts with grains near the surface, while only a small fraction penetrates deeper through intergranular gaps. The EDS analysis shows an enrichment of Sr element near the surface, accompanied by a large reduction of Cu content. This suggests that the rod-like grains near the surface are most likely $SrCO_3$. In a previous study,[52] the formation of rod-like $SrCO_3$ due to the reaction between CO_2 and $Sr(OH)_2$ solution was reported. The reaction kinetics under low CO_2 and high H_2O partial pressures lead to an anisotropic growth of $SrCO_3$ along *c*-axis, which is consistent with the rod-like particles observed in our water-treated samples.

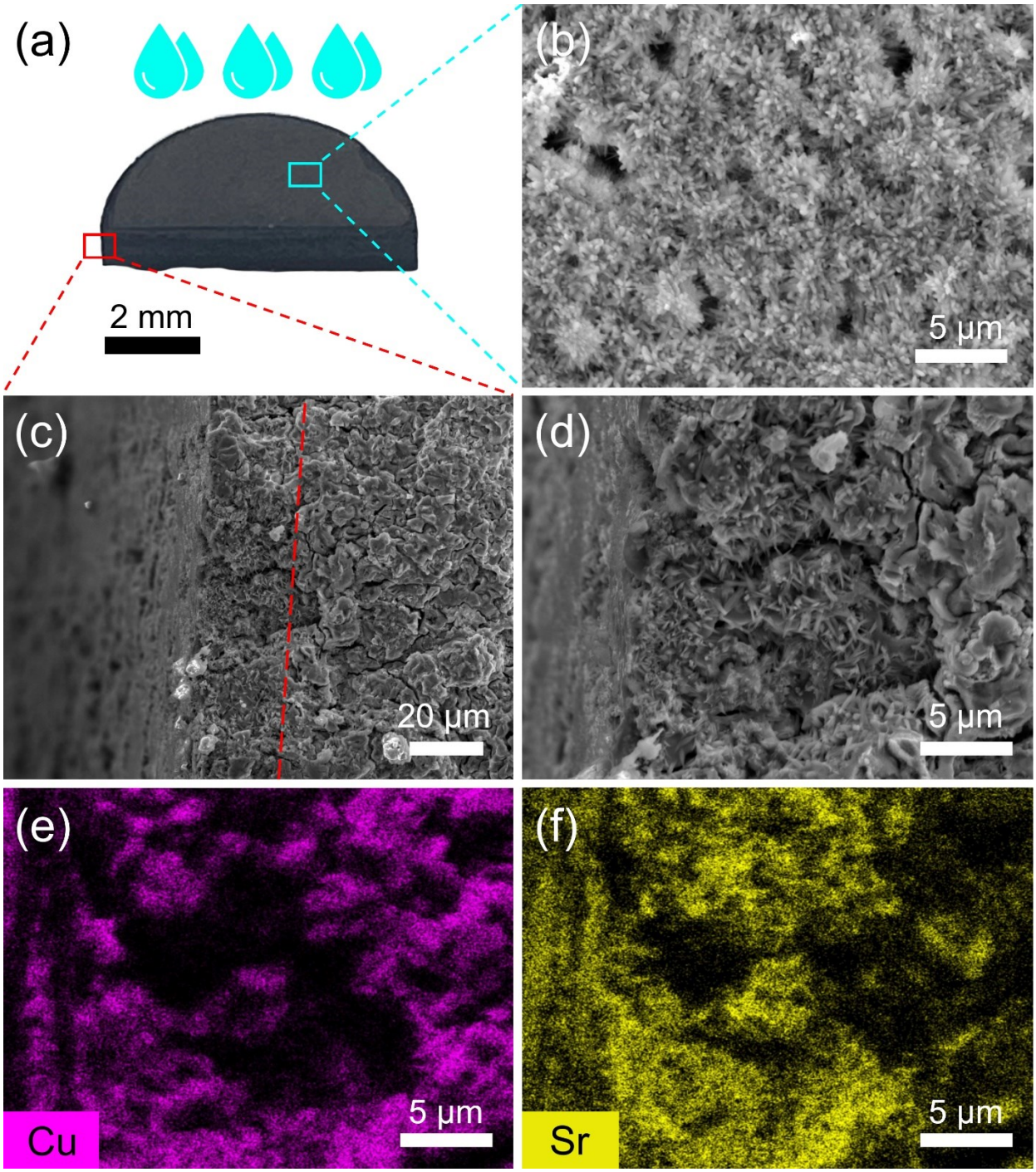

Fig. 3 (a) A photo of the polycrystalline $Sr_{12}Y_2Cu_{24}O_{41}$ pellet prepared by cold pressing. (b) SEM image taken on the surface of $Sr_{12}Y_2Cu_{24}O_{41}$ after 10 h water treatment. (c) SEM image taken near the edge of $Sr_{12}Y_2Cu_{24}O_{41}$ after 10 h water treatment. The red dash line indicates approximate boundary between two distinct particle morphologies. (d) Zoomed in SEM image on (c). (e) and (f) EDS mapping results of Cu and Sr element on (d), respectively.

Effect of water treatment on thermal conductivity of uncoated $Sr_{12}Y_2Cu_{24}O_{41}$

The thermal conductivity data of the samples after water treatment for 0, 1, 4, and 10 h are shown in Fig. 4a. A significant decrease in thermal conductivity is observed as the treatment duration increases from 0 to 4 h. The thermal conductivity at 300 K was reduced from 2.3 W m^{-1} K^{-1} for the pristine sample to 1.5 W m^{-1} K^{-1} for the 4 h sample. However, extending the treatment duration to 10 h results in minimal further reduction, indicating that the reaction rate between water and the spin ladder compound slows significantly beyond 4 h. We calculate the solid thermal conductivity (κ_S) by correcting the porosity effect with:[41,53]

$$\kappa_s = \kappa \frac{2+\Phi}{2-2\Phi}, \tag{5}$$

where the porosity Φ is 15% for the cold-pressed samples. We assume that the porosity of the samples is approximately the same after water treatment. The solid thermal conductivity is shown in Fig. 4b. Due to the large energy gap of magnons (32.5 meV) in spin ladder compounds,[11] the magnon thermal conductivity is negligible below 50 K.[29] Therefore, the thermal transport at low temperatures is dominated by phonons, allowing us to fit the data using the Callaway model. The fitting parameters obtained from this low-temperature analysis are subsequently extrapolated to higher temperatures to estimate the lattice thermal conductivity (κ_L) across the entire temperature range. The magnon thermal conductivity is subsequently determined by subtracting the phonon contribution from the total measured thermal conductivity. This approach effectively characterizes the phonon background and has been used in prior studies to separate the magnon contribution in spin ladder compounds.[29,31,37,41]

The Callaway model for lattice thermal transport can be expressed as:[31,54]

$$\kappa_L = \frac{k_B}{2\pi^2 v_s}\left(\frac{k_B T}{\hbar}\right)^3 \int_0^{\frac{\theta_D}{T}} \frac{x^4 e^x}{\tau^{-1}(e^x-1)^2}\,\mathrm{d}x, \tag{6}$$

where k_B is the Boltzmann constant, v_s is the sound velocity in the spin ladder compound, $\hbar$ is the reduced Planck constant, T is the temperature, θ_D is the Debye temperature, and $x = \frac{\hbar\omega}{k_B T}$, which acts as a variable of integration. The phonon relaxation time τ can be affected by several scattering processes, including the phonon-defect scattering (τ_d), phonon-boundary scattering (τ_b), phonon-phonon Umklapp scattering (τ_U) and nanoparticle scattering (τ_{np}). According to Matthiessian's law, τ can be expressed as:[55]

$$\tau^{-1} = \tau_d^{-1} + \tau_U^{-1} + \tau_b^{-1} + \tau_{np}^{-1} = A\omega^4 + B\exp\left(-\frac{b}{T}\right)T^3\omega^2 + \frac{v_s}{L} + \tau_{np}^{-1}, \tag{7}$$

where A is the fitting parameter for defect scattering, B and b are the fitting parameters for Umklapp scattering, and L is the phonon-boundary scattering mean free path. The term τ_{np}^{-1} accounts for the nanoparticle scattering and is given by:[56]

$$\tau_{np}^{-1} = v_{\mathrm{np}} N_p \left[(2\pi R^2)^{-1} + \left(\frac{4}{9}\pi R^2 \left(\frac{D_M - D_P}{D_M}\right)^2 \left(\frac{\omega R}{v_{np}}\right)^4\right)^{-1}\right]^{-1}, \tag{8}$$

where v_{np}, N_p, and R are the sound velocity, concentration, and radius of the nanoparticles, respectively. D_M and D_P are the mass density of matrix and nanoparticle, respectively. The value of R is 200 nm,

estimated from the SEM images. N_p is the fitting parameter for nanoparticle scattering. The obtained fitting parameters are listed in Table 1, which are comparable to the results reported in previous studies.[31,38]

Table 1. Fitting parameters of the Callaway model

	Pristine	1 h	4 h	10 h
$A(\mathrm{s}^3)$	2.7627×10^{-41}	2.7756×10^{-41}	2.8268×10^{-41}	2.8448×10^{-41}
$B(\mathrm{s\ K}^{-3})$	2.0021×10^{-17}	2.0059×10^{-17}	2.0016×10^{-17}	2.004×10^{-17}
b (K)	154.3538	155.7805	152.5979	154.0235
L (m)	3.5485×10^{-7}	3.5487×10^{-7}	5.0488×10^{-7}	5.0488×10^{-7}
N_p (m^{-3})	0	1×10^{19}	2.3×10^{19}	2.3×10^{19}

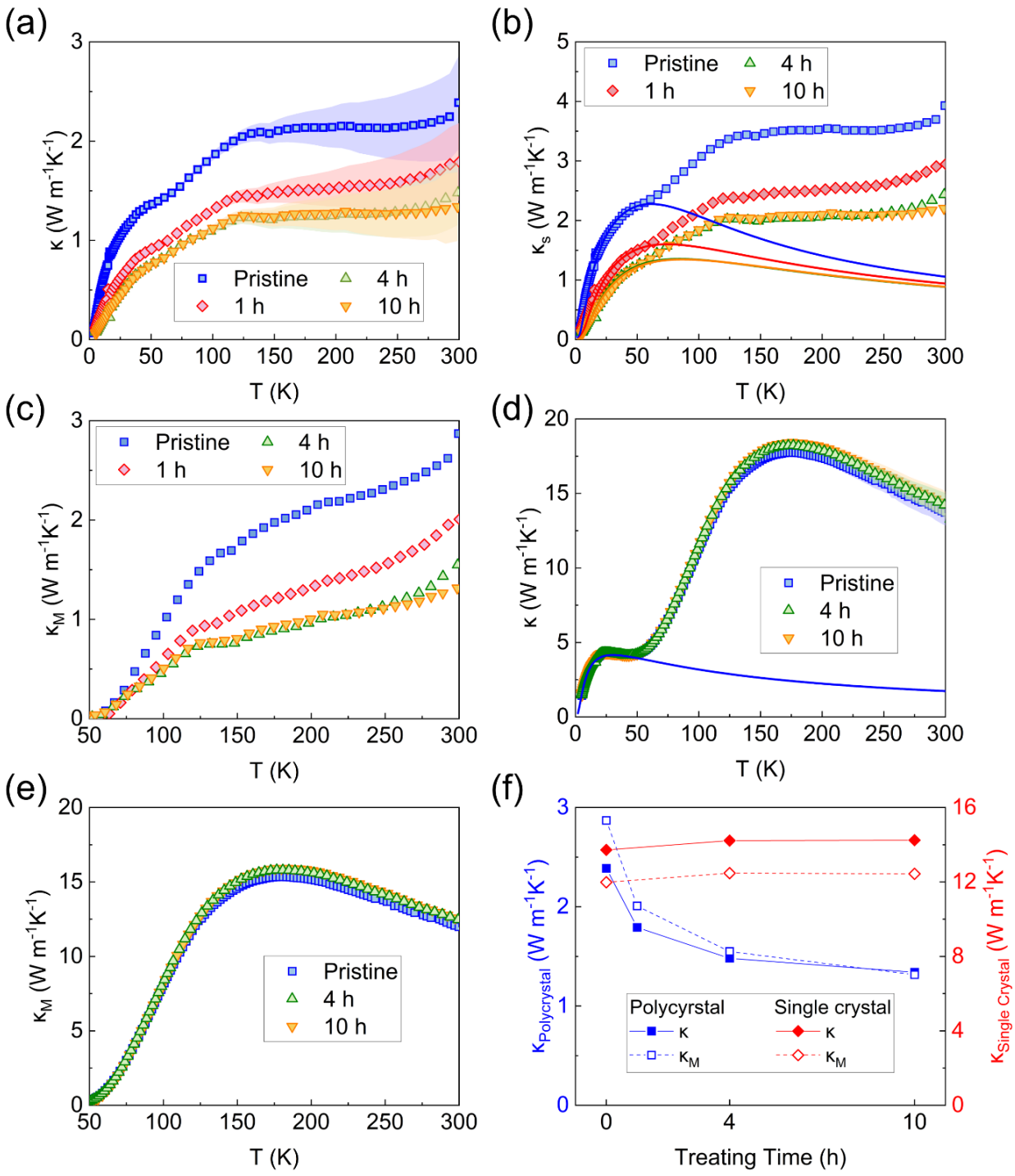

Fig. 4 (a) Measured thermal conductivity, (b) solid thermal conductivity, and (c) magnon thermal conductivity of polycrystalline $Sr_{12}Y_2Cu_{24}O_{41}$ with various water treating time. The shaded area in (a) depicts the measurement error of thermal conductivity. Lines in (b) are fitted lattice thermal conductivity based on Equ. (6). (d) Measured thermal conductivity and (e) magnon thermal conductivity of single crystal $Sr_{12}Y_2Cu_{24}O_{41}$ with various water treating time. Lines in (b) and (d) are fitted lattice thermal conductivity based on Equ. (6) without considering nanoparticle scattering. (f) Treating time dependence of thermal conductivity of polycrystalline and single-crystal $Sr_{12}Y_2Cu_{24}O_{41}$ at 300 K.

The magnon thermal conductivity is extracted by subtracting the lattice thermal conductivity, estimated by the Callaway model, from the solid thermal conductivity, as shown in Fig. 4c. Both phonon and magnon thermal conductivity exhibit similar trends with respect to the treating time. As the treating time increases to 4 h, both lattice and magnon thermal conductivity decrease monotonically. At around 50 K, the peak value of the lattice thermal conductivity decreases from 2.3 to 1.3 W m^{-1} K^{-1}. At the same time, the value of magnon thermal conductivity at 300 K decreases from 2.8 to 1.3 W m^{-1} K^{-1}, which is an over 50% reduction. This substantial suppression of both lattice and magnon thermal conductivity indicates that the nanostructures, formed during the decomposition process, effectively scatter both phonons and magnons. Extending the treating time from 4 to 10 h results in only a marginal further reduction in thermal conductivity. This diminished rate of reaction is likely due to the reduced contact between water and the spin ladder compound, as the decomposition products form a barrier that hinders further interaction.

We further study the effect of water treatment on the thermal transport in single crystal $Sr_{12}Y_2Cu_{24}O_{41}$. In contrast to the behavior observed in the polycrystals, the thermal conductivity of the single crystal shows minimal dependence on the treating time. As shown in Fig. 4d and e, both lattice and magnon thermal conductivity exhibit negligible changes even after 10 h treatment. This observation indicates that the decomposition process of the spin ladder compound is negligible in the single crystal. Fig. 4f compares the time-dependence of measured thermal conductivity and magnon thermal conductivity at 300 K for both polycrystal and single crystal. In the polycrystal, the thermal conductivity reduces exponentially with increasing treating time, suggesting a deceleration in the reaction rate between water and the spin ladder compound. This phenomenon is caused by the formation of nanoparticles, which reduces the gaps between boundaries and prevents water from penetrating deep into the sample. In the single crystal, due to the absence of grain boundaries, there is no pathway for water to penetrate into the sample. Thus, decomposition only happens in the region near the surface, which constitutes only a small portion of the sample and causes little effect on the thermal conductivity. It is worth comparing the thermal conductivity of our samples with that of commercial ceramics. At room temperature, the thermal conductivity of our samples is about 2.3 W m^{-1} K^{-1} for the polycrystal and 14.2 W m^{-1} K^{-1} for the single crystal. These values are significantly higher—by 50% and 850%, respectively—than those of commercial porcelain and other ceramics, which typically have thermal conductivity in the range of 0.5-1.5 W m^{-1} K^{-1}.[57–59]

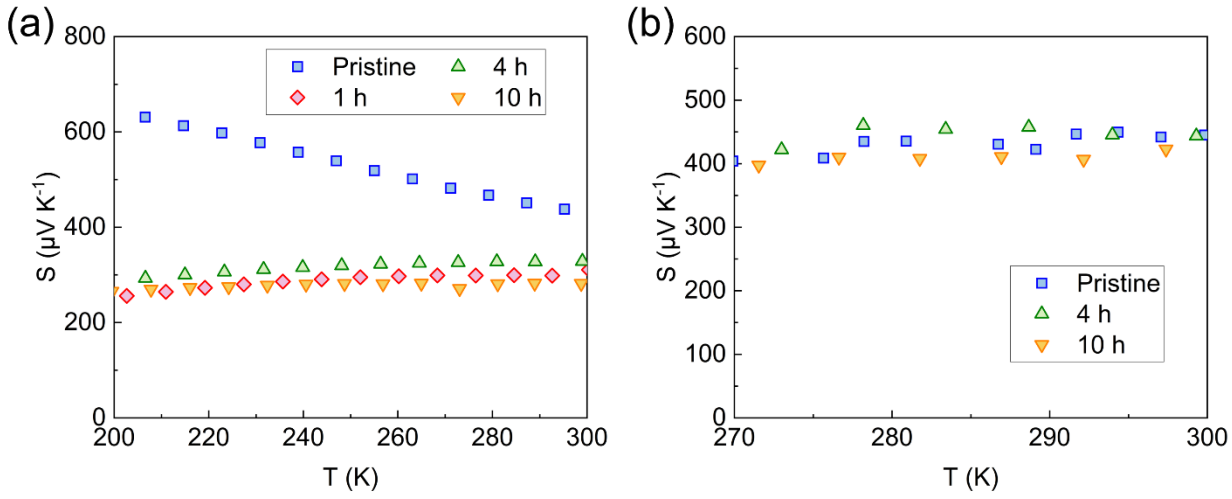

Fig. 5 (a) Seebeck coefficient of $Sr_{12}Y_2Cu_{24}O_{41}$ polycrystal with various water treating time. (b) Seebeck coefficient of $Sr_{12}Y_2Cu_{24}O_{41}$ single crystal along *c*-axis with various water treating time.

We further studied the Seebeck coefficient of the samples with different water treating time. As shown in Fig. 5a, a large reduction in the Seebeck coefficient can be observed in the $Sr_{12}Y_2Cu_{24}O_{41}$ polycrystal. At room temperature, the Seebeck coefficient of the pristine sample reaches about 430 μV K^{-1}. However, after water treatment, the Seebeck coefficient is suppressed to about 350 μV K^{-1}. The appearance of the nanostructured CuO and $SrCO_3$ may have altered the electrical properties of the sample,[60–62] leading to the increased hole concentration and the suppression of Seebeck coefficient.[63,64] Additionally, the Seebeck coefficient of the pristine simple shows a decreasing trend with increasing temperature, which is a typical non-degenerate semiconductor behavior, while the water treated samples shows a weaker temperature dependence. On the other hand, the Seebeck coefficient of the single crystal sample remains nearly unchanged before and after water treatment, maintaining approximately 430 μV K^{-1} at 300 K.

Effect of water treatment on thermal conductivity and microstructure of metal coated polycrystalline $Sr_{12}Y_2Cu_{24}O_{41}$

To prevent the decomposition of the spin ladder compounds in the humid environment, a polycrystalline spin ladder sample was coated with a thin layer of gold using a sputtering method. This gold layer, approximately 100 nm in thickness, serves as a protective barrier against moisture. As illustrated in Fig. 6, the adverse effects of water treatment on thermal conductivity were significantly mitigated by this coating. After 50 h of exposure to water treatment, the thermal conductivity of the sputtered sample remained nearly unchanged compared to that of the pristine sample, indicating the effectiveness of the protective layer.

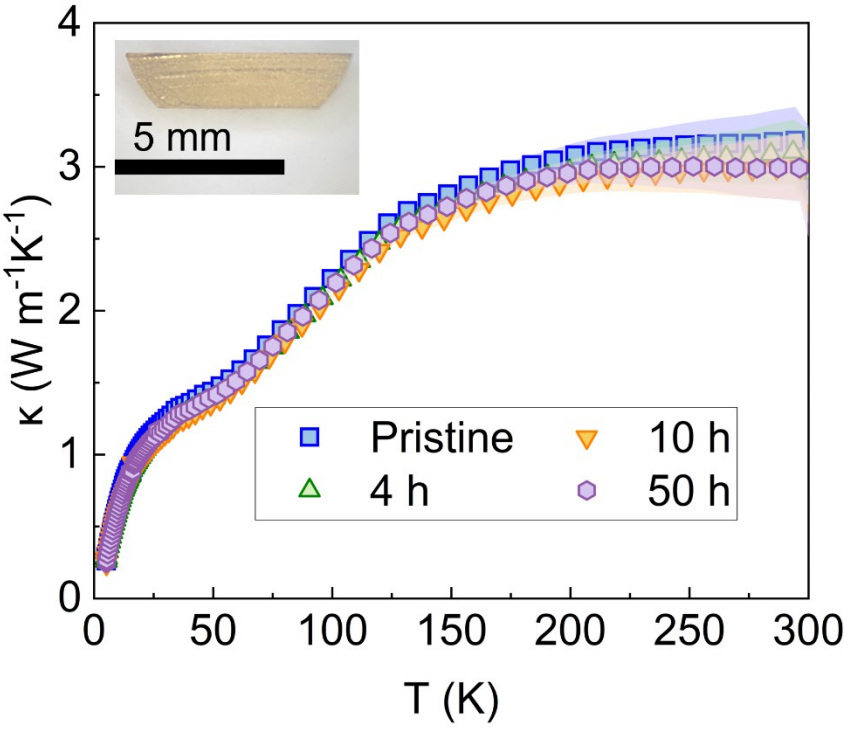

Fig. 6 Measured thermal conductivity of the sputtered $Sr_{12}Y_2Cu_{24}O_{41}$ after water treatment. The inset is the optical photo of the sputtered sample. The shaded area depicts the measurement error of thermal conductivity.

Furthermore, SEM images of both the center and edge of the treated sample, as shown in Fig. 7, reveal a smooth surface with well-defined grains, similar to those observed in the pristine polycrystalline material. These observations underscore the effectiveness of the gold sputter coating in shielding the sample from water-induced degradation. Overall, the results demonstrate that the gold coating not only preserves the structural integrity of the spin ladder compounds but also maintains their thermal properties, making it a promising approach for enhancing the durability of these materials in humid conditions.

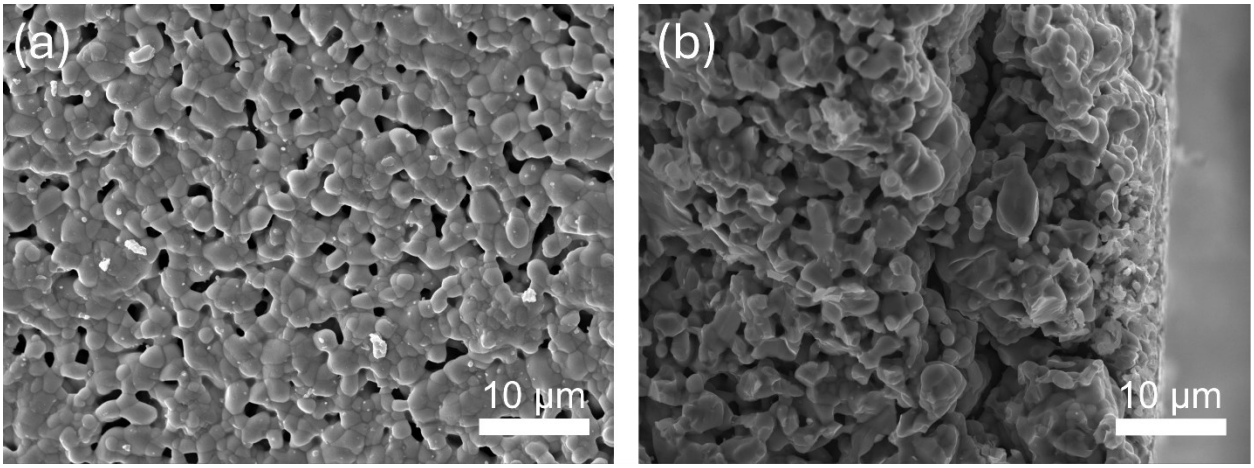

Fig. 7 SEM images of the gold-coated $Sr_{12}Y_2Cu_{24}O_{41}$ polycrystal taken (a) on the center and (b) around the edge, respectively.

Conclusions

We investigated the effects of water exposure on the microstructure and thermal transport in water-sensitive spin ladder compound $Sr_{12}Y_2Cu_{24}O_{41}$. The combined effect of water treatment and drying in air leads to the formation of impurity nanostructures. Near the surface, an enrichment of $SrCO_3$ nanorods is observed, while both $SrCO_3$ and CuO nanoparticles form at the center of polycrystal, resulting in significant deformation of particle morphology as compared to the pristine sample. The introduction of nanostructures results in a significant 50% reduction of both lattice and magnon thermal conductivity in the polycrystal subjected to 4 h of water treatment. Specifically, the maximum lattice thermal conductivity is reduced from 2.6 to 1.3 $W\ m^{-1}\ K^{-1}$ at around 40 K. At room temperature, the magnon thermal conductivity is reduced from 2.8 to 1.3 $W\ m^{-1}\ K^{-1}$. Further extending the treatment duration reveals only minimal additional effects, indicating a decreased reaction rate between the water and the spin ladder compounds. The formation of nanoparticles tends to fill the gaps between the material's structures, thereby hindering the diffusion of water deeper into the sample. Additionally, the effect of water treatment also leads to the suppression of the Seebeck coefficient, which indicates the changes in the overall electrical properties of the sample due to the formation of the nanostructured CuO and $SrCO_3$. Conversely, the effect of water treatment on the thermal conductivity is negligible in the single crystals and metal-coated polycrystals, even after more than 10 h of water treatment. This result shows that the absence of grain boundaries in single crystals or a protective coating layer in polycrystals prevents water from penetrating deeply into the material, thereby preserving its thermal properties. Our findings provide valuable insights into the impact of water-induced decomposition on magnon thermal transport in spin ladder compounds, an area previously unexplored. Furthermore, we have established a simple and cost-effective metal-coating technique to protect these

water-sensitive materials from moisture, ensuring long-term durability. Our research significantly enhances potential applications of the spin ladder compounds for thermal management and energy conversion.

Author contributions

Shuchen Li: Conceptualization (support); Formal analysis (lead); Investigation (lead); Writing – original draft (lead); Writing – review & editing (equal). **Xi Chen**: Conceptualization (lead); Supervision (lead); Funding acquisition (lead); Writing – review & editing (equal)

Conflicts of interest

The authors have no conflicts to disclose.

Data availability

The data that support the findings of this study are available from the corresponding author upon reasonable request.

ACKNOWLEDGMENTS

This work was supported by the National Science Foundation under grant number 2144328.

References

1 A. L. Moore and L. Shi, *Materials Today*, 2014, 17, 163–174.

2 Z. Liu, X. Yang, B. Zhang and W. Li, *ACS Appl Mater Interfaces*, 2021, 13, 53409–53415.

3 G. Pan, Y. Yao, X. Zeng, J. Sun, J. Hu, R. Sun, J.-B. Xu and C.-P. Wong, *ACS Appl Mater Interfaces*, 2017, 9, 33001–33010.

4 T. Swoboda, K. Klinar, A. S. Yalamarthy, A. Kitanovski and M. Muñoz Rojo, *Adv Electron Mater*, 2021, 7, 2000625.

5 Y. Li, W. Li, T. Han, X. Zheng, J. Li, B. Li, S. Fan and C.-W. Qiu, *Nat Rev Mater*, 2021, 6, 488–507.

6 S. Hou, B. Sun, F. Tian, Q. Cai, Y. Xu, S. Wang, X. Chen, Z. Ren, C. Li and R. B. Wilson, *Adv Electron Mater*, 2022, 8, 2200017.

7 J. S. Kang, M. Li, H. Wu, H. Nguyen and Y. Hu, *Science (1979)*, 2018, 361, 575–578.

8 F. Tian, B. Song, X. Chen, N. K. Ravichandran, Y. Lv, K. Chen, S. Sullivan, J. Kim, Y. Zhou, T.-H. Liu, M. Goni, Z. Ding, J. Sun, G. A. G. Udalamatta Gamage, H. Sun, H. Ziyaee, S. Huyan, L. Deng, J. Zhou, A. J. Schmidt, S. Chen, C.-W. Chu, P. Y. Huang, D. Broido, L. Shi, G. Chen and Z. Ren, *Science (1979)*, 2018, 361, 582–585.

9 S. Berber, Y.-K. Kwon and D. Tománek, *Phys Rev Lett*, 2000, 84, 4613–4616.

10 K. Chen, B. Song, N. K. Ravichandran, Q. Zheng, X. Chen, H. Lee, H. Sun, S. Li, U. G. G. A. Gamage, F. Tian, Z. Ding, Q. Song, A. Rai, H. Wu, P. Koirala, A. J. Schmidt, K. Watanabe, B. Lv, Z. Ren, L. Shi, D. G. Cahill, T. Taniguchi, D. Broido and G. Chen, *Science (1979)*, 2020, 367, 555–559.

11 X. Chen, D. Bansal, S. Sullivan, D. L. Abernathy, A. A. Aczel, J. Zhou, O. Delaire and L. Shi, *Phys Rev B*, 2016, 94, 134309.

12 R. Steinigeweg, J. Herbrych, X. Zotos and W. Brenig, *Phys Rev Lett*, 2016, 116, 017202.

13 C. Hess, H. ElHaes, B. Büchner, U. Ammerahl, M. Hücker and A. Revcolevschi, *Phys Rev Lett*, 2004, 93, 027005.

14 G. T. Hohensee, R. B. Wilson, J. P. Feser and D. G. Cahill, *Phys Rev B*, 2014, 89, 024422.

15 A. V. Sologubenko, K. Giannò, H. R. Ott, A. Vietkine and A. Revcolevschi, *Phys Rev B*, 2001, 64, 054412.

16 N. Hlubek, X. Zotos, S. Singh, R. Saint-Martin, A. Revcolevschi, B. Büchner and C. Hess, *Journal of Statistical Mechanics: Theory and Experiment*, 2012, 2012, P03006.

17 X. Chen, J. Carrete, S. Sullivan, A. van Roekeghem, Z. Li, X. Li, J. Zhou, N. Mingo and L. Shi, *Phys Rev Lett*, 2019, 122, 185901.

18 D. R. Ratkovski, L. Balicas, A. Bangura, F. L. A. Machado and S. M. Rezende, *Phys Rev B*, 2020, 101, 174442.

19 N. Prasai, B. A. Trump, G. G. Marcus, A. Akopyan, S. X. Huang, T. M. McQueen and J. L. Cohn, *Phys Rev B*, 2017, 95, 224407.

20 D. S. Inosov, Y. O. Onykiienko, Y. V. Tymoshenko, A. Akopyan, D. Shukla, N. Prasai, M. Doerr, D. Gorbunov, S. Zherlitsyn, D. J. Voneshen, M. Boehm, V. Tsurkan, V. Felea, A. Loidl and J. L. Cohn, *Phys Rev B*, 2020, 102, 184431.

21 J. Jia, S. Li, X. Chen and Y. Shigesato, *Adv Funct Mater*, 2024, 2406667.

22 N. Terakado, Y. Nara, Y. Machida, Y. Takahashi and T. Fujiwara, *Sci Rep*, 2020, 10, 14468.

23 K. Uchida, S. Takahashi, K. Harii, J. Ieda, W. Koshibae, K. Ando, S. Maekawa and E. Saitoh, *Nature*, 2008, 455, 778–781.

24 H. Adachi, K. Uchida, E. Saitoh and S. Maekawa, *Reports on Progress in Physics*, 2013, 76, 036501.

25 J. Xiao, G. E. W. Bauer, K. Uchida, E. Saitoh and S. Maekawa, *Phys Rev B*, 2010, 81, 214418.

26 Md. M. H. Polash, F. Mohaddes, M. Rasoulianboroujeni and D. Vashaee, *J Mater Chem C Mater*, 2020, 8, 4049–4057.

27 Y. Zheng, T. Lu, M. M. H. Polash, M. Rasoulianboroujeni, N. Liu, M. E. Manley, Y. Deng, P. J. Sun, X. L. Chen, R. P. Hermann, D. Vashaee, J. P. Heremans and H. Zhao, *Sci Adv*, 2019, 5, eaat9461.

28 M. R. Natale, D. J. Wesenberg and B. L. Zink, *Phys Rev Mater*, 2024, 8, 044402.

29 C. Hess, C. Baumann, U. Ammerahl, B. Büchner, F. Heidrich-Meisner, W. Brenig and A. Revcolevschi, *Phys Rev B*, 2001, 64, 184305.

30 C. Hess, C. Baumann and B. Büchner, *J Magn Magn Mater*, 2005, 290–291, 322–325.

31 A. V Sologubenko, K. Giannó, H. R. Ott, U. Ammerahl and A. Revcolevschi, *Phys Rev Lett*, 2000, 84, 2714–2717.

32 H. Pan, Z.-K. Ding, B.-W. Zeng, N.-N. Luo, J. Zeng, L.-M. Tang and K.-Q. Chen, *Phys Rev B*, 2023, 107, 104303.

33 M. Matsuda, K. Katsumata, R. S. Eccleston, S. Brehmer and H.-J. Mikeska, *J Appl Phys*, 2000, 87, 6271–6273.

34 C. Hess, B. Büchner, U. Ammerahl, L. Colonescu, F. Heidrich-Meisner, W. Brenig and A. Revcolevschi, *Phys Rev Lett*, 2003, 90, 197002.

35 X. F. Sun, J. Takeya, S. Komiya and Y. Ando, *Phys Rev B*, 2003, 67, 104503.

36 S. Guo, X. Bai, B. Liang, T. Hoke, M. Liu, R. E. Dunin-Borkowski and X. Chen, *Adv Funct Mater*, 2024, 2417505.

37 C. Hess, U. Ammerahl, C. Baumann, B. Büchner and A. Revcolevschi, *Physica B Condens Matter*, 2002, 312–313, 612–613.

38 S. Li, S. Guo, Y. Wang, H. Li, Y. Xu, V. Carta, J. Zhou and X. Chen, *J Appl Phys*, 2024, 136, 045105.

39 K. Naruse, T. Kawamata, M. Ohno, Y. Matsuoka, K. Kumagai and Y. Koike, *Solid State Commun*, 2013, 154, 60–63.

40 X. Chen, J. Kim, Q. Jia, S. E. Sullivan, Y. Xu, K. Jarvis, J. Zhou and L. Shi, *Adv Funct Mater*, 2020, 30, 2001637.

41 X. Chen, K. Jarvis, S. Sullivan, Y. Li, J. Zhou and L. Shi, *Phys Rev B*, 2017, 95, 144310.

42 S. Li, S. Guo, Y. Xu, J. Zhou and X. Chen, *ACS Appl Electron Mater*, 2022, 4, 787–794.

43 S. Guo, H. Li, X. Bai, Y. Wang, S. Li, R. E. Dunin-Borkowski, J. Zhou and X. Chen, *Cell Rep Phys Sci*, 2024, 5, 101879.

44 H. Tian, C. Ren and S. Wang, *Nanotechnology*, 2022, 33, 212001.

45 A. V Sologubenko, T. Lorenz, H. R. Ott and A. Freimuth, *J Low Temp Phys*, 2007, 147, 387–403.

46 J. M. Hill, D. C. Johnston and L. L. Miller, *Phys Rev B*, 2002, 65, 134428.

47 U. Ammerahl and A. Revcolevschi, *J Cryst Growth*, 1999, 197, 825–832.

48 X. Hu, Y. Zhao, X. Shen, A. V. Krasheninnikov, Z. Chen and L. Sun, *ACS Appl Mater Interfaces*, 2020, 12, 26367–26373.

49 T. Siegrist, L. F. Schneemeyer, S. A. Sunshine, J. V Waszczak and R. S. Roth, *Mater Res Bull*, 1988, 23, 1429–1438.

50 P. Scherrer, *Nach Ges Wiss Gottingen*, 1918, 2, 8–100.

51 U. Holzwarth and N. Gibson, *Nat Nanotechnol*, 2011, 6, 534–534.

52 J. Hong, S. J. Heo and P. Singh, *Sci Rep*, 2021, 11, 3368.

53 D. S. Smith, A. Alzina, J. Bourret, B. Nait-Ali, F. Pennec, N. Tessier-Doyen, K. Otsu, H. Matsubara, P. Elser and U. T. Gonzenbach, *J Mater Res*, 2013, 28, 2260–2272.

54 S. Guo, Y. Xu, T. Hoke, G. Sohi, S. Li and X. Chen, *J Appl Phys*, 2023, 133, 120701.

55 J. Callaway, *Physical Review*, 1959, 113, 1046–1051.

56 J. Lei, K. Zhao, J. Liao, S. Yang, Z. Zhang, T.-R. Wei, P. Qiu, M. Zhu, L. Chen and X. Shi, *Nat Commun*, 2024, 15, 6588.

57 E. García, A. de Pablos, M. A. Bengoechea, L. Guaita, M. I. Osendi and P. Miranzo, *Ceram Int*, 2011, 37, 369–375.

58 J. García Ten, M. J. Orts, A. Saburit and G. Silva, *Ceram Int*, 2010, 36, 1951–1959.

59 D. G. Cahill, J. R. Olson, H. E. Fischer, S. K. Watson, R. B. Stephens, R. H. Tait, T. Ashworth and R. O. Pohl, *Phys Rev B*, 1991, 44, 12226–12232.

60 Ş. Baturay, A. Tombak, D. Batibay and Y. S. Ocak, *Appl Surf Sci*, 2019, 477, 91–95.

61 T. Jiang, M. Bujoli-Doeuff, Y. Farré, Y. Pellegrin, E. Gautron, M. Boujtita, L. Cario, S. Jobic and F. Odobel, *RSC Adv*, 2016, 6, 112765–112770.

62 X.-Y. Hou, J. Tan, C.-E. Hu, X.-R. Chen and H.-Y. Geng, *Phys Lett A*, 2021, 390, 127083.

63 D. Michael. Rowe, *Thermoelectrics handbook : macro to nano*, CRC/Taylor & Francis, 2006.

64 L. Su, H. Shi, S. Wang, D. Wang, B. Qin, Y. Wang, C. Chang and L. Zhao, *Adv Energy Mater*, 2023, 13, 2300312.